Quasimonochromatic Bright Gamma-ray Generation from Synchronized Compton Scattering via Azimuthal Spatial-Temporal Coupling

Xuesong Geng,[1] Liangliang Ji,[1,*] and Baifei Shen[1,2,†]

[1] *State Key Laboratory of High Field Laser Physics and CAS Center for Excellence in Ultra-intense Laser Science, Shanghai Institute of Optics and Fine Mechanics (SIOM), Chinese Academy of Sciences (CAS), Shanghai 201800, China*

[2] *Shanghai Normal University, Shanghai 200234, China*

(Received 15 July 2021; revised 17 November 2021; accepted 24 January 2022; published 18 February 2022)

High-energy photons can be generated via inverse Compton scattering (ICS) in the collision between energetic electrons and an intense laser pulse. The development of laser plasma accelerators promises compact and all-optical gamma-ray sources by colliding the electrons from laser wakefield accelerators with high-power driving pulses reflected by a plasma mirror. However, the law of optical focusing hinders realization of both high photon yield and monochromatic spectra in this scenario. We propose an azimuthal spatial-temporal convertor that decouples the focal field strength from laser spot size using helical parabolic geometry. It decomposes the driving laser beam into a pulse train of almost identical divergence angle and focal depth, creating synchronized ICS in the optimized linear regime. The scheme resolves the dilemma between high efficiency and narrow energy spread, facilitating the generation of monochromatic gamma rays using high power lasers beyond relativistic field strengths.

DOI: 10.1103/PhysRevApplied.17.024055

I. INTRODUCTION

Photons in the gamma-ray regime can stimulate photonuclear reactions, providing a powerful tool to probe the dynamics in nuclei. To this end, it is often required that the gamma-ray beam is monochromatic with sufficient photon flux to selectively excite the nuclear states [1]. This has been a major quest in developing nuclear photonics but faces significant challenges. Synchrotron radiation [2–6] and free-electron lasers [7–9] have been quite successful in providing bright light sources up to the hard-x-ray regime. However, it is unlikely that state-of-the-art techniques can be extended to the gamma-ray regime. Instead, abundant gamma photons can be efficiently produced via bremsstrahlung [10], where the photon spectra usually follow an exponential decay distribution, and the beam is rather divergent [11]. On the other hand, the inverse Compton scattering (ICS) [12,13] mechanism promises highly directional gamma-ray beams with narrow energy spread, via low energy laser photons scattered off relativistic electrons. They gain a maximum $4\gamma^2$ (where γ is the electron Lorentz factor) boost to the laser frequency and become blue shifted [14,15].

Various ICS gamma-ray sources have been realized worldwide in conventional accelerators [16–19] or via laser-driven wakefield accelerated (LWFA) electrons [20–22]. The latter process is particularly promising since it generates ultrabright ultrafast gamma-ray flashes in a compact all-optical scenario. Laser-based ICS is usually facilitated via the reflection-collision geometry: the high-power femtosecond laser pulse driving wakefield acceleration also serves as the collision laser after reflection by a plasma mirror. This approach takes full advantage of the ultrahigh photon density provided by the driving laser and resolves the synchronization issue between the laser and electron beams [22–26].

The typical photon number generated in ICS is about 10^7–10^9 per pulse [22,23,27], which is much smaller than that from bremsstrahlung (about 10^{10}–10^{11}). One may increase the light intensity of the scattering laser in ICS to boost the photon yield. However, this is limited by the nonlinear threshold. When the field strength of the collision laser exceeds $a_0 = 1$, ICS enters the nonlinear or the multiphoton absorption regime, where the gamma-ray spectrum is red shifted and broadened [28–30]. Here $a_0 = E_0 e/\omega mc$ denotes the nonlinearity of the collision process, with E_0 the laser electric field magnitude, e the unit charge, ω the laser frequency, m the electron mass, and c the speed of light. In other words, there exists a dilemma between photon yield and spectrum width. Take a typical 50 TW, 30 fs laser pulse in LWFA as an example. The linear ICS ($a_0 < 1$) requires a beam waist larger than $w_0 \approx 40$ μm as shown in red in Fig. 1(a). On the other hand, photon yield is optimized at high laser intensities when the Rayleigh

*jill@siom.ac.cn
†bfshen@mail.shcnc.ac.cn

length is comparable to the pulse length $z_R \sim c\tau$, corresponding to $w_0 \approx 1$ μm in the grey area of Fig. 1(a). However, focusing the laser to a small spot size of $w_0 \approx 1$ μm results in higher field strength and broadening of the ICS spectrum. Therefore, the gap between high photon yield and low bandwidth cannot be bridged using ordinary focusing optics, for instance, a parabolic plasma mirror [31–33].

We propose a solution to the dilemma using a spatial-temporal coupling geometry. Here a parabolic mirror is azimuthally decomposed into N sections and stretched along the laser axis with a chosen spacing d, forming a helical parabolic mirror, as illustrated in Fig. 2(a). When impinging onto the divided parabola, a fraction of the incident laser pulse is reflected and focused to the collision point in every period of time. Adjacent subparabolas are displaced by a distance of d; therefore, the time at which each subpulse arrives at its focus is delayed by d/c. One can see in Figs. 2(b) and 2(c) that a train of identical subpulses is generated with intensity peak shifting backwards along the electron beam. Each carries the same field amplitude below unity. The proposed geometry is essentially an azimuthal spatial-temporal (AST) convertor that decouples the focal field strength from laser spot size such that the light intensity from every focusing element can be programmed to assure linear ICS and the matching condition between the beam waist and the electron beam radius. Since each focal point is no longer fixed but is moving against the laser propagation direction at the speed of light, it is synchronized with the trailing electron beam [see Fig. 2(c)] to guarantee the optimized collision set in Fig. 1(b): the monochromatic requirement $a_0 = 1$, and the saturation condition $z_R \sim c\tau$.

It has been shown that spatial-temporal coupling can be realized via spatial-dispersive lenses [34,35], axially delayed mirrors [36], and axial parabolas [37,38], offering a superluminal laser focus—a promising approach to drive dephasingless wakefield acceleration [36]. All existing spatial-temporal concepts essentially depend on radially delayed focusing, namely, the radial spatial-temporal (RST) convertor, which can be simplified to the structure illustrated in Fig. 3(b). The subpulses generated by these axially symmetric parabolas are reflected or transformed at different radii, therefore having different divergences and focal depths or Rayleigh lengths, e.g., $z_R^{(3)} > z_R^{(2)} > z_R^{(1)}$ in Fig. 3(b) where $z_R = \pi w_0^2/\lambda$ is the Rayleigh length and w_0 is the beam waist. Thus, in either LWFA or ICS only a few subpulses work in optimal conditions because the pulse Rayleigh length should match the plasma density required for optimal LWFA conditions [39,40] and the pulse divergence angles should remain constant for monochromatic gamma beams in ICS. However, the majority do not match. Unlike in the RST geometry, the proposed AST convertor in principle generates identical subpulses with the same spot size, field strength, and polarization near the axis, as shown in Fig. 3(a), providing identical colliding pulses for the Compton scattering and an invariant driving pulse for LWFA, hence ensuring optimized interaction for all subpulses.

II. RESULTS

The idea is demonstrated by considering the ICS process between a 500 MeV electron beam and a driving laser pulse with $a_0 = 2$ and wavelength of 800 nm. The electron beam contains a total charge of 4.4 pC distributed in a cylinder of 0.5 μm in radius and 2 μm in length, corresponding to 1% energy spread and 1 mrad angular divergence [41,42]. Their interaction is mimicked in full three-dimensional (3D) particle-in-cell (PIC) simulations to include the diffraction effects and the laser-plasma interactions at such extreme fields. The radiation from Compton scattering is calculated by resolving the Lienard-Wiechert

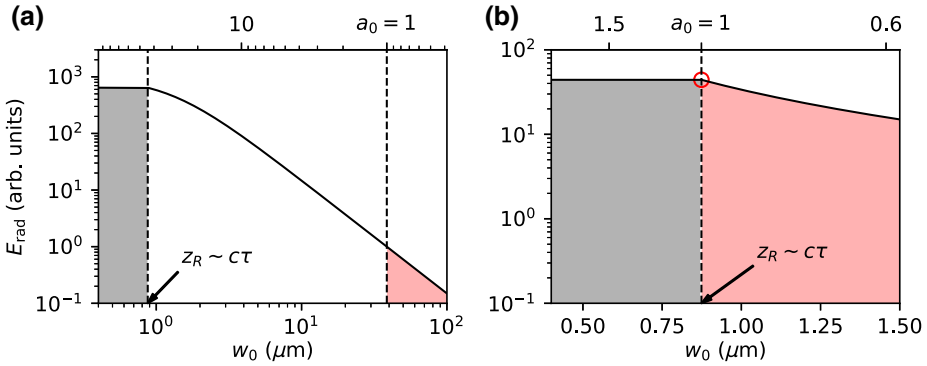

FIG. 1. The schematic of the relation between the radiation yield E_{rad} in ICS and the beam waist of the colliding laser pulse w_0 for a 50 TW, 30 fs laser in the case of ordinary optical focusing (a) and spatial-temporal coupling (b), as a function of the beam waist and field strength. The radiation yield is normalized to that of $a_0 = 1$. In either case, yield saturates from $z_R \sim c\tau$ (gray) while the linear ICS corresponds to $a_0 \leq 1$ (red). Optimal gamma radiation is achieved for $a_0 = 1$ and $z_R \sim c\tau$, as shown by the red circle in (b).

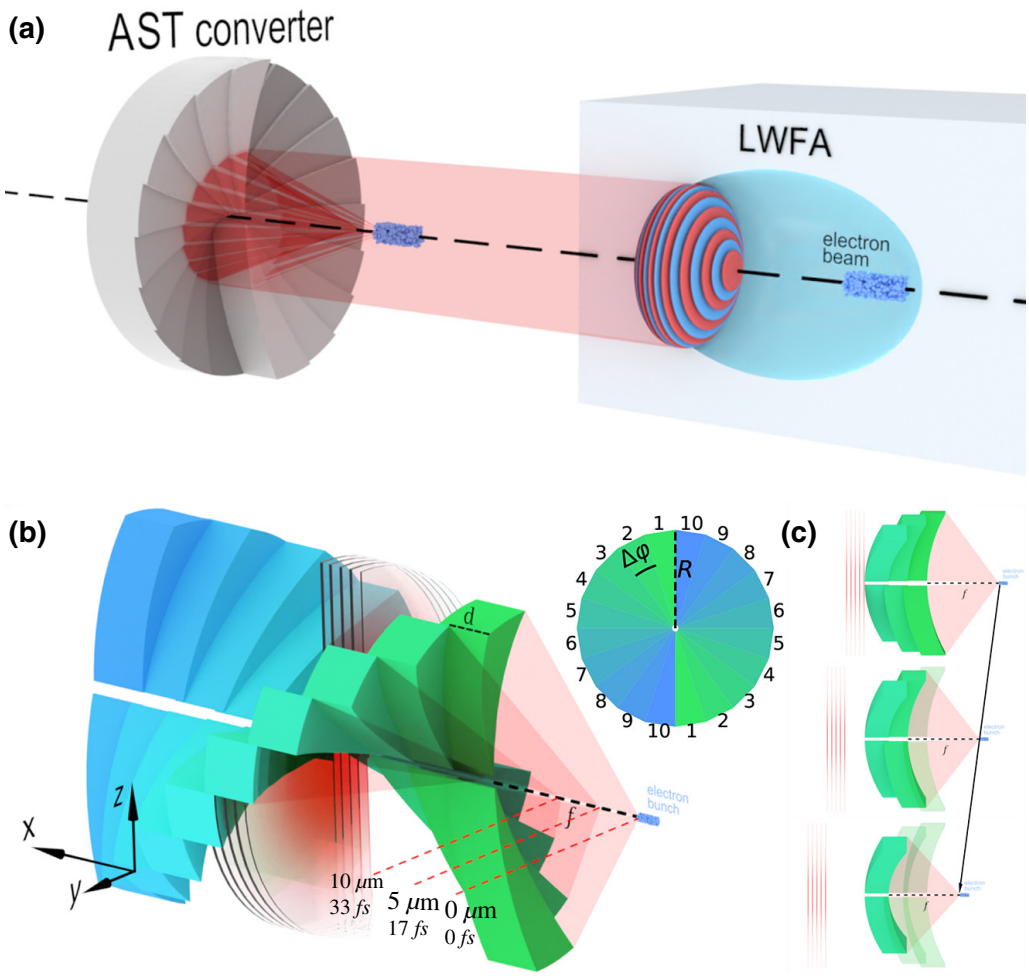

FIG. 2. The AST coupling geometry. (a) The schematic geometry of the collision of an electron beam from LWFA with a pulse train reflected by the AST convertor. (b) The mirror structure and subpulses during reflection (green for nearer; blue for further). The front view of the mirror is shown in the upper right. (c) The synchronized collision between the electron beam and the first three subpulses with focal position moving inversely to its wave vector at the speed of light. Each mirror component is subdivided into a pair to assure symmetric collision force along the transverse directions.

potential of each traced electron (see Sec. IV). For synchronization of the trailing electron and reflected laser pulse, we constrain the laser spot size to $w_0 = 10\ \mu$m and set the focal length of the reflecting mirror to be $f = 30\ \mu$m. For a typical LWFA configuration, such a driving laser pulse of $a_0 = 2$ and pulse duration of 27 fs corresponds to a peak power of 13.4 TW and beam energy of 358 mJ.

We compare the results with the quasi-plane-wave and the parabolic plasma mirror with fixed focus. For the latter, the trailing electron beam is displaced by $l_e = 2f = 60\ \mu$m with respect to the laser pulse, ensuring a matched collision. Note that the distance l_e can be varied by controlling the LWFA conditions, such as plasma density and laser spot size [40]. The on-axis photon energy from linear ICS with 500 MeV electrons is 5.94 MeV. In general, the central beam energy is lower than the on-axis value after integrating over a range of emitting angles. The intense laser field can also induce significant red shift. In the flat-mirror geometry [see Figs. 4(a)–4(c)], electrons undergo oscillations at a peak field strength of $a_0 = 2$, a typical field strength employed in the single-pulse reflection-collision geometry [22]. It produces a broadened and red-shifted spectrum, peaking at 3.88 MeV with bandwidth of $\Delta\varepsilon_\gamma = 9.32$ MeV at FWHM (full width at half maximum), and divergence angle of $\Delta\theta \approx 2.61$ mrad (FWHM). Overall, the energy radiated is $E_{\rm rad} = 1.05 \times 10^7$ MeV/pC, corresponding to about $N_\gamma = E_{\rm rad}/\varepsilon_\gamma \approx 1.18 \times 10^6$ photons/pC.

The highest yield is expected when focusing the whole pulse onto one spot with a parabolic mirror of $f = 30\ \mu$m (equivalent to an AST convertor with $N = 1$ mirror pair). In this case, the focal field strength is magnified by an order of 12.5 to $a_0 \approx 25$. Although this produces a much higher radiated energy, $E_{\rm rad} = 6.76 \times 10^8$ MeV/pC, the strong nonlinear effect and radiation recoil result in an extremely red-shifted spectrum, $\varepsilon_{\rm peak} \approx 0.47$ MeV. Photons are emitted to a much larger divergence angle $\Delta\theta \approx 3.72$ mrad. The energy bandwidth is $\Delta\varepsilon_\gamma = 5.41$ MeV, containing abundant low-energy photons as shown in Figs. 4(d) and 4(f), corresponding to $N_\gamma = 1.05 \times 10^8$ photons/pC when counting gamma-ray photons with energies greater than 1 MeV.

When switching to the AST geometry, the proposed azimuthal structure generates subpulses of similar duration and field strength that are fully synchronized with the

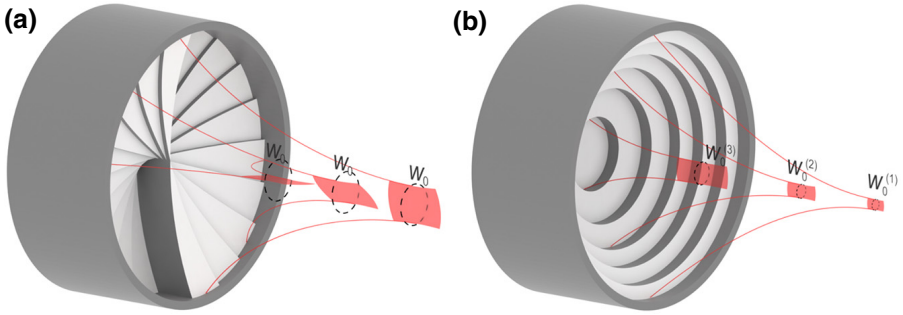

FIG. 3. AST convertor generates subpulses of identical focal length (a), while RST convertor produces different focal lengths for each subpulse (b).

collision process [see in Fig. 4(g)]. Fourteen subpulses are aligned in Fig. 4(h) carrying a maximum field amplitude of $a_0 \approx 1$, where $N = 15$ mirror pairs are utilized and the first mirror pair is flattened to remove the first pulse that is beyond $a_0 = 1$, which will be discussed in Sec. III B. Consequently, electrons experience a period of oscillation that is about 14 times longer under the same field strength compared with the quasi-plane-wave case. The radiation yield is boosted to $E_{\mathrm{rad}} = 1.53 \times 10^7$ MeV/pC, corresponding to $N_\gamma = 3.43 \times 10^6$ photons/pC peaking at 4.47 MeV. The bandwidth is suppressed to $\Delta\varepsilon_\gamma = 1.31$ MeV, which is a sevenfold suppression of the flat mirror geometry. The photon beam is much more collimated to $\Delta\theta \approx 1.35$ mrad, as shown in Fig. 4(i). In terms of brilliance, measured by $N_\gamma/(\Delta\varepsilon_\gamma \Delta\theta^2)$, the AST convertor reaches 1.08×10^6 photons/pC/MeV/mrad^2, which is almost 60 times more than the flat mirror geometry that produces 1.86×10^4 photons/pC/MeV/mrad^2.

On the other hand, considering the laser efficiency, the AST convertor produces 9.58×10^6 photons/pC/J at 4.47 MeV out of a 358-mJ-laser pulse, which is 21 times 4.5×10^5 photons/pC/J at up to 1 MeV out of a laser pulse of 0.13 J and $a_0 = 0.3$ [43], 63 times 1.5×10^5 photons/pC/J at 15 keV out of a laser pulse of 300 mJ

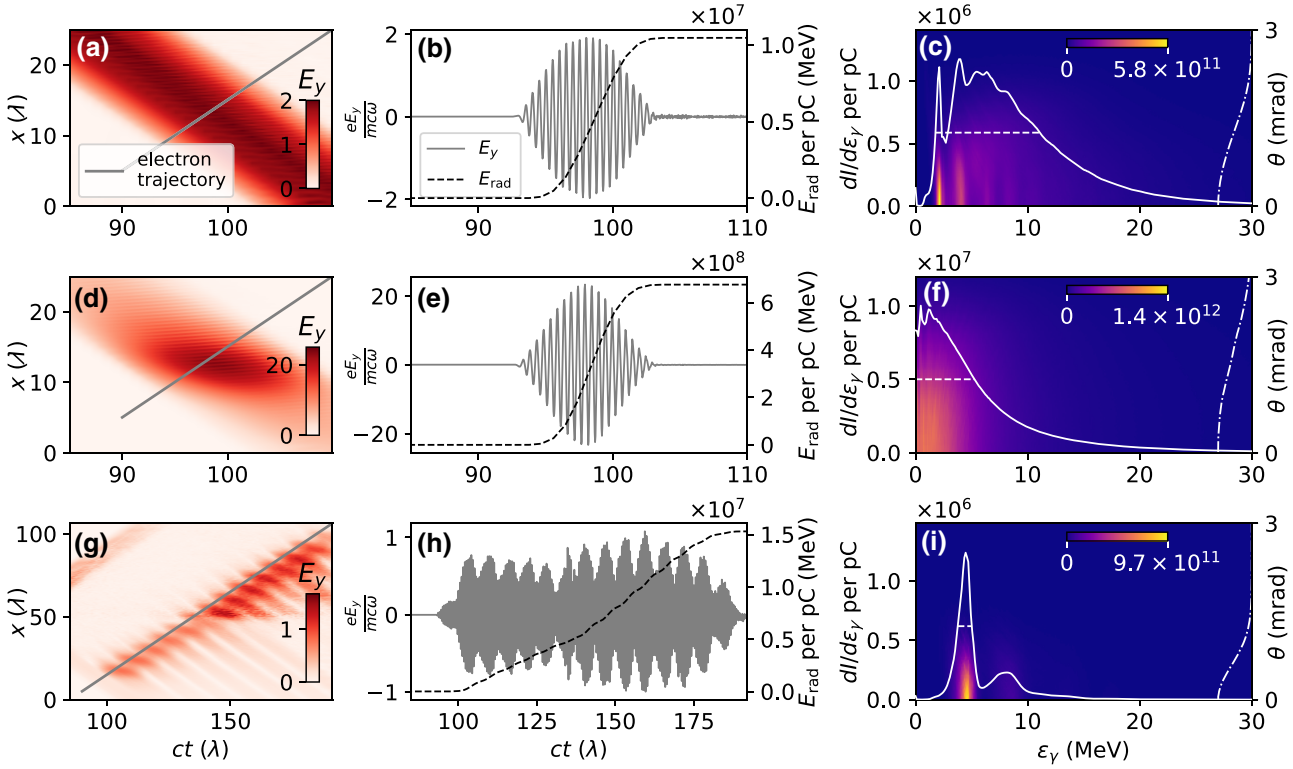

FIG. 4. Field strengths and ICS spectra. (a) The on-axis field strengths E_y reflected by a flat mirror; (b) the electric fields experienced by an electron on the axis (solid gray line), corresponding to the gray line in (a) and the radiation yield of the electron beam (dashed black line); (c) the produced spectrum $d^2I/d\varepsilon_\gamma d\Omega$ per pC in units of rad^{-2} where the solid white lines are the energy spectra $dI/d\varepsilon_\gamma$ and the dashed white lines are the FWHM and the peak photon energy. (d)–(f) The results for a full parabolic mirror. (g)–(i) The results for AST geometry where the first mirror pair is set flat.

and $a_0 = 0.85$ [44], and 17 times 5.05×10^5 photons/pC/J at up to 2 MeV out of a 3.3 J laser pulse of $a_0 = 1.3$ [23].

Comparing the three cases, it is obvious that the AST geometry realizes linear ICS using full laser power, which is otherwise prohibited by single-focus optics. It successfully boosts the radiation yield and retains the quasimonochromatic feature. In addition, the beam collimation is also greatly improved.

III. DISCUSSION AND CONCLUSION

A. Scaling law of the mirror pairs

The photon spectra of different mirror pair numbers N are presented in Fig. 5(a). The peak photon energy increases for higher N and the bandwidth is narrowed simultaneously. The spectrum exhibits a quasimonochromatic feature starting from $N = 10$ and the energy spread is further suppressed by flattening the first mirror pair (labeled "without first pair"), which will be explained in the next section. From Figs. 5(b) and 5(c), we find that the brilliance of the AST convertor peaks at $N = 15$ where the spectrum bandwidth and beam collimation are also optimized. Here high energy photon radiation is hindered for the undivided parabolic mirror ($N = 1$) case, as the electron energy is significantly depleted due to the radiation reaction. This leads to a relatively small bandwidth but at the cost of a strong red shift and loss of high-energy photons. The radiation yield is also dependent on the focal length. One sees the highest radiation energy around $f \approx 27\ \mu$m, shown in Fig. 5(d), which is a slight shift from the designed $f = 30\ \mu$m, because we use a Gaussian pulse of $w_0 = 10\ \mu$m in simulations, which is not an ideal plane wave. As for the central photon energy and bandwidth, both remain stable for different focal lengths, as shown in Figs. 5(d) and 5(e). We notice that the trend in Fig. 5(d) indicates a focal window of about 6 μm at FWHM. This defines the tolerance on focusing fluctuation in the current setup.

B. Diffraction loss from the mirror pairs

We further discuss the diffraction effect present in the AST geometry. The wave fronts of the incident laser pulse during interaction with the AST convertor and the on-axis field strengths are shown in Figs. 6(a)–6(d) for $N = 15$ and Figs. 6(e)–6(h) for $N = 5$. The first mirror pair experience an undisturbed wave front, after which the wave front is then disturbed by a diffraction effect from the finite size of

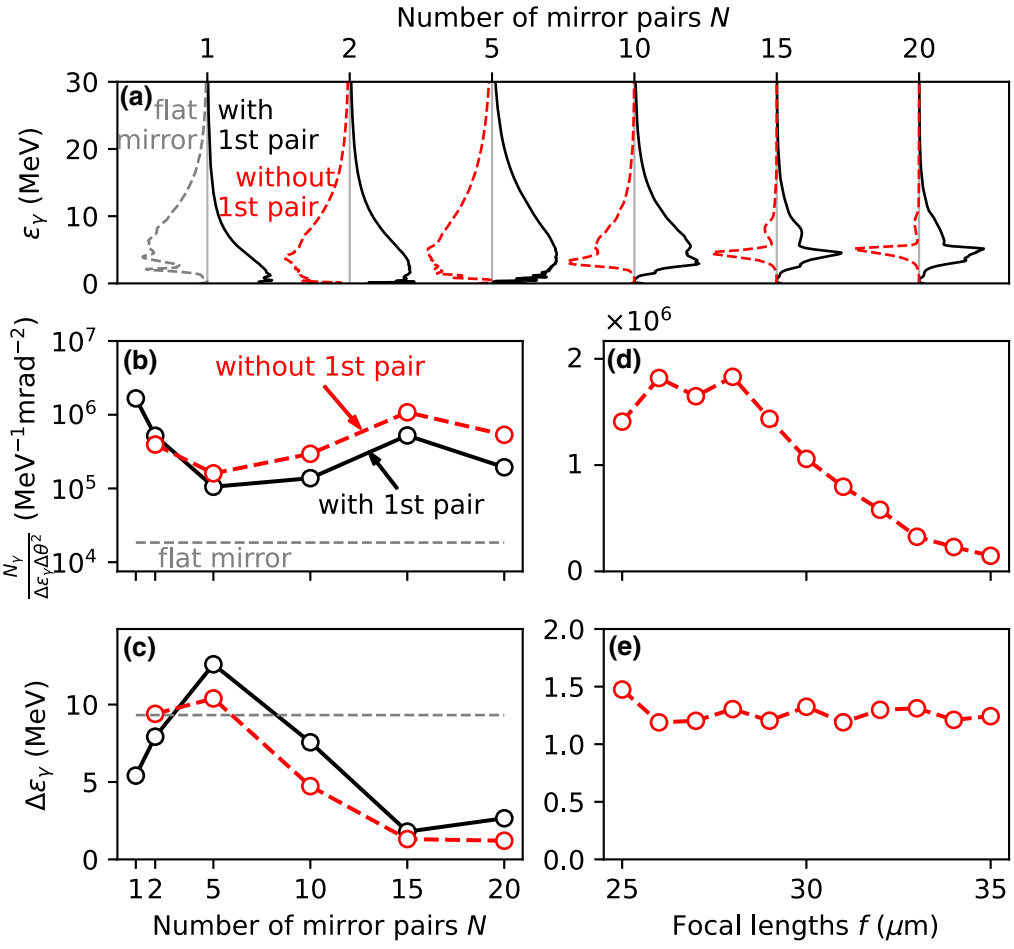

FIG. 5. The scaling law for the number of parabolic mirror pairs. (a) Spectra for different pair numbers. The black lines denote AST convertors with the first mirror pairs; the dashed red lines denote AST convertors with the first pairs flattened; the dashed gray line is the result of the flat mirror. (b) The radiation brilliance measured by $dN_\gamma/\Delta\varepsilon_\gamma\Delta\theta^2$ per pC, (c) the bandwidth $\Delta\varepsilon_\gamma$. The solid black (dashed red) lines are the results with (without) the first mirror pairs, and the dashed gray line corresponds to the flat mirror. (d) and (e) The results for different focal lengths of $N = 15$ corresponding to (b) and (c).

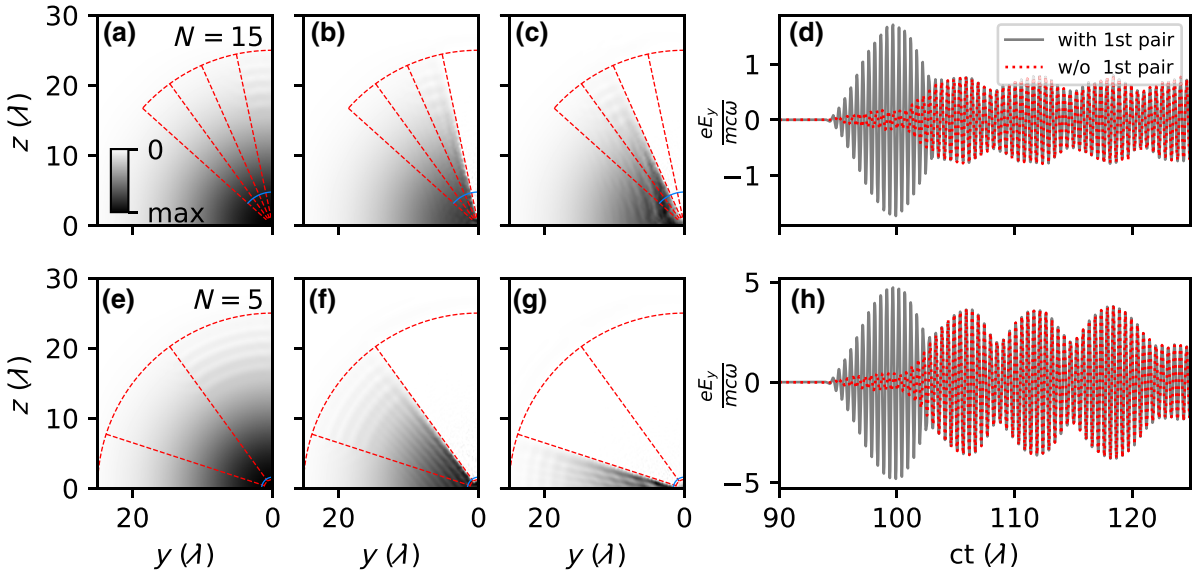

FIG. 6. Wave fronts of the incident laser and on-axis field strengths. (a)–(c) The field strengths in the plane of phase 0 and (d) on-axis field strengths for (a)–(d) $N = 15$ mirror pairs and (e)–(h) $N = 5$ mirror pairs. The dashed-red lines in (a)–(c) and (e)–(h) are the outlines of the mirrors and the blue arcs indicate the radius when the arc length of a mirror equals the laser wavelength, which measures the region of strong diffraction effect. The dotted red (solid black) lines in (d) and (h) are the on-axis field strengths experienced by an electron with (without) the first mirror pair flattened.

the mirror pairs and the pulses are relatively weaker than the first pulse, as shown by the black lines in Figs. 6(d) and 6(h). The diffraction is stronger for smaller mirror pairs, as indicated by the difference between the amplitudes. We then flatten the first mirror pair to eliminate the nonlinear effect induced by the first subpulse. Such a microstructure can be fabricated via 3D printing techniques [45] for experimental consideration.

C. Diffraction loss during focusing

Taking into account the diffraction effect, the field strengths of the subpulses for different pair numbers are shown in Fig. 7. The f number of a parabolic mirror is $f_{\mathcal{N}} = f/2R$ where R is the mirror radius. For an undivided parabolic mirror, the focal spot size should be about $\lambda f_{\mathcal{N}}$. For a parabolic mirror pair, the radial size remains $2R$ but the azimuthal size decreases to about $2R/N$, which expands the focal spot size in the azimuthal direction to about $\lambda[f/(2R/N)] = \lambda N f_{\mathcal{N}}$. Because each subpulse shares $1/N$ of the laser power, $P \sim a_0^2 w_0^2 \sim 1/N$, and w_0 scales as $w_0^2 \sim \lambda f_{\mathcal{N}} \times \lambda N f_{\mathcal{N}} \sim N$, the focal field strength therefore scales as $1/N$. In other words, the finite size of the mirror pairs and consequent diffraction produce a scaling of about $1/N$ (dashed black line in Fig. 7) rather than $1/\sqrt{N}$. From another point of view, since the Maxwell equation is linear, the focal field of an undivided parabolic mirror can be linearly decomposed into multiple combinations of fields from the subdivisions of the mirror, which are the mirror pairs of the AST convertor. Therefore, the focal field strengths of the subpulses can be predicted by

$$a_0^{\mathrm{foc}}(N) = \frac{a_0^{\mathrm{foc}}(1)}{N}, \tag{1}$$

which is exactly the black dashed line in Fig. 7. The above relationship provides a simple rule to design the structure of an AST convertor for high-quality gamma-ray beam generation by requiring $N \sim a_0^{\mathrm{foc}}(1)$.

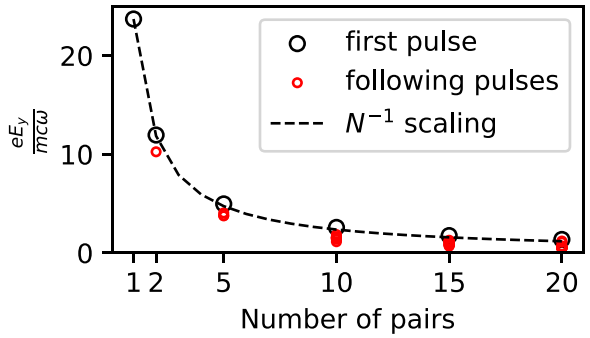

FIG. 7. The on-axis field strengths of the pulse train for different numbers of mirror pairs. The black circle denotes the field strength of the first subpulse and the smaller red circles denote the following pulses. The dashed line represents the field strengths fitted with $1/N$.

D. General applications

For more general purposes, the AST convertor can be scaled to larger sizes to interact with laser pulses below the

damage threshold of the mirror; this also makes it easier to fabricate. In this geometry, an independent pulse can be used in the collision with the electron bunch, relaxing the constraints on the laser pulse from the output of the LWFA process. Furthermore, this geometry redistributes the laser energy and generates comoving focuses behind the laser pulse, satisfying the requirements of applications like dephasingless LWFA [36] and ponderomotive-controlled radiation [46]. For micrometer-scale AST convertors, the microstructure can be manufactured with state-of-the-art 3D-printing techniques [45], and can be collimated by detecting signals passing through the passage for the electron beam [see Fig. 2(b)].

In conclusion, the proposed AST geometry can transform the incident laser pulse into a train of almost identical pulses, controlling the field strength below the nonlinear threshold of the ICS process without compromising the radiation yield in the all-optical Compton source. It significantly suppresses the bandwidth of the generated radiation spectrum and achieves a monochromatic output.

IV. METHODS

A. Estimation of radiation yield

The radiation yield in Fig. 1 is estimated by integrating the radiation-reaction force in the collision between an electron of $\gamma_0 = 1000$ and a laser pulse of 30 fs at FWHM. For highly relativistic electrons ($\gamma \gg 1$), the radiation-reaction force, taken from the Landau-Lifshitz equation [14], is approximated by

$$\mathbf{F}_{\mathrm{RR}} \approx -\frac{2}{3}\frac{e^4}{m^2c^5}\gamma^2\left[(\mathbf{E}+\mathbf{v}\times\mathbf{B})^2-(\beta\cdot\mathbf{E})^2\right]\mathbf{v}, \quad (2)$$

where $\beta = \mathbf{v}/c$ and $\mathbf{v}$ is the electron velocity. Since $\gamma \gg a_0$ is considered, the electron motion in the laser field is simplified to a one-dimensional trajectory and $\mathbf{F}_{\mathrm{RR}} \approx -(8/3)(e^2\omega^2/c^2)\gamma^2 a_0^2\mathbf{v}$. The radiation power becomes $d\gamma mc^2/dt = \mathbf{F}_{\mathrm{RR}}\cdot\mathbf{v} \approx -(8/3)(e^2\omega^2/c)\gamma^2 a_0^2(t)$ where $a_0(t)$ is the field strength experienced by the electron, which is then integrated to

$$\int_{\gamma_0}^{\gamma_f}\gamma^{-2}d\gamma = -\frac{8}{3}\frac{e^2\omega^2}{mc^3}\int_{t_i}^{t_f}a_0^2(t)dt = -I(t_i,\ t_f),$$

and, finally, we have $\gamma_f = [\gamma_0^{-1} + I(t_i,\ t_f)]^{-1}$. The radiation yield is estimated by $(\gamma_0 - \gamma_f)\ mc^2$. The integration limits are determined by the interaction period that decreases to $2z_R/c$ when the Rayleigh length is smaller than the pulse length for extremely tight focusing, which results in the saturation plateau in Fig. 1.

B. Simulation setup

The simulation is carried out via the SMILEI code [47] with a cell size of $0.05\lambda \times 0.17\lambda \times 0.17\lambda$ in the x, y, and z dimensions with the laser pulse in the x direction. The size of the simulation box is adjusted for different numbers of mirror pairs so long as the mirror plus its focal length can fit into the simulation domain. For example, the box size is $117.6\ \times 44\ \times 44\ \mu$m for $N = 15$ mirror pairs, corresponding to $2940 \times 320 \times 320$ grids.

The AST convertor with focal length of $f = 30\ \mu$m is set to be preionized in the simulation and its electron number density is $100n_c$ with 16 macroparticles per cell. Here $n_c = \varepsilon_0 m\omega^2/e^2$ is the critical plasma density with ε_0 being the vacuum permittivity. The convertor is generated by subdividing a parabolic mirror into $2N$ sections, or N opposite pairs, and displacing adjacent mirror pairs by $d = 5\ \mu$m. A tunnel of radius of 1 μm through the mirror is reserved for electron propagation.

The electron beam enters the simulation box from the boundary along the x axis following the laser pulse. The pulse profile is defined by $a_0 \sin(\pi t/2\tau)e^{-r^2/w_0^2}$ where $a_0 = 2$, $w_0 = 10\ \mu$m, and $\tau = 27$ fs. The spacing between the beam and the peak of the laser profile is $l_e = 2f$, required by the time delay introduced by parabolic mirror. The central energy of the electron beam is 500 MeV with 1% energy spread and angular divergence of 1 mrad at e^{-1} of a Gaussian profile. The electron beam is uniformly distributed in a cylinder of 0.5 μm in radius and 2 μm in length, which represents 4.4 pC (4.65 pC in the simulation owing to the grid effect) of electrons, corresponding to the number density of 1.744×10^{25} m^{-3} with 10 macroparticles per cell. Take LWFA for example: the spacing l_e between the laser peak and the beam center is dependent on the size of the bubble r_b [40] as the electron beam is accelerated at the tail of the bubble. This spacing can be tuned by changing the LWFA conditions, e.g., the plasma density n_0, the field strength a_0, and the beam waist w_0 of the driving laser.

C. Radiation spectrum

The radiation fields are obtained by calculating the Lienard-Wiechert potential [15] in specific directions following the electron trajectories $(\mathbf{x}, \mathbf{p})$ from PIC simulations

$$\mathbf{E} \approx \frac{e}{c^2R}\frac{\mathbf{n}\times\left[\left(\mathbf{n}-\frac{\mathbf{v}}{c}\right)\times\dot{\mathbf{v}}\right]}{\left(1-\mathbf{n}\cdot\frac{\mathbf{v}}{c}\right)^3}, \quad (3)$$

where R is the distance from the electron to the observation point, $\mathbf{n}$ is the direction to the observation point, $\mathbf{v}$ the velocity of electron, and $\dot{\mathbf{v}}$ the acceleration. The right-hand side is evaluated at time steps of electron and the left-hand side is defined at time steps of $t' = t + R/c$. Then we calculate the spectrum via Fourier transformation of the electric fields in the time domain. Since t' depends on $R(t)$ and is not uniformly distributed, we first interpolate the radiation fields on a uniform time grid, then we perform fast Fourier

transformation to the interpolated radiation fields. One can refer to the thesis [48] for numerical details.

Since the pulse length of the radiation fields are compressed by a factor of $4\gamma^2$ compared to the laser pulse length, i.e., $c\tau/4\gamma^2 \sim 2$ pm, much smaller than the average distance between electrons, i.e., $n_e^{-1/3} \approx 4$ nm, the radiation is highly incoherent for highly relativistic electrons and the spectrum of each trajectory can be simply summed up without considering coherence effects.

The electron trajectories taken from PIC simulations inherently include the radiation-reaction effect in Eq. (2). This is necessary for the case of $a_0 = 25$. For electron energy of $\gamma = O(10^3)$ and field strength of $a = O(1)$, we have the quantum parameter [49] $\chi = O(10^{-2})$, which indicates the nonlinear quantum effects are weak [50–52]. Therefore, classical calculations are sufficient to deal with the radiation spectrum. In the case of $a_0 \approx 25$ and $\chi_e \approx 0.15$, where quantum effects may arise, we find the classical estimation does not deviate much from the QED Monte-Carlo calculation of the SMILEI code. For consistency, we keep the classical calculations in our results.

ACKNOWLEDGMENTS

We acknowledge funding from National Science Foundation of China (Grants No. 11875307, No. 11935008, and No. 11804348); and Strategic Priority Research Program of Chinese Academy of Sciences (Grant No. XDB16010000).

[1] C. R. Howell, *et al.*, International workshop on next generation gamma-Ray source, J. Phys. G: Nucl. Part. Phys. **49**, 010502 (2021).
[2] F. R. Elder, R. V. Langmuir, and H. C. Pollock, Radiation from electrons accelerated in a synchrotron, Phys. Rev. **74**, 52 (1948).
[3] I. M. Ternov, Synchrotron radiation, Phys.-Usp. **38**, 409 (1995).
[4] S. S. R. Lightsource (SSRL), As a National User Facility the Stanford Synchrotron Radiation Lightsource Invites Scientists from All over the World to Use Our Intense X-Ray Beam and World-Class Instruments for Their Experiments, http://www-ssrl.slac.stanford.edu/content
[5] DESY PHOTON SCIENCE, https://photon-science.desy.de/
[6] HZDR – Helmholtz-Zentrum Dresden-Rossendorf, https://www.hzdr.de
[7] J. M. J. Madey, Stimulated emission of bremsstrahlung in a periodic magnetic field, J. Appl. Phys. **42**, 1906 (1971).
[8] FLASH, https://photon-science.desy.de/facilities/flash/index_eng.html
[9] European XFEL, https://www.xfel.eu
[10] T. ERBER, High-Energy electromagnetic conversion processes in intense magnetic fields, Rev. Mod. Phys. **38**, 626 (1966).
[11] S. Li, B. Shen, J. Xu, T. Xu, Y. Yu, J. Li, X. Lu, C. Wang, X. Wang, X. Liang, Y. Leng, R. Li, and Z. Xu, Ultrafast multi-MeV gamma-Ray beam produced by laser-accelerated electrons, Phys. Plasmas **24**, 093104 (2017).
[12] R. H. Milburn, Electron Scattering by an Intense Polarized Photon Field, Phys. Rev. Lett. **10**, 75 (1963).
[13] F. R. Arutyunian and V. A. Tumanian, The compton effect on relativistic electrons and the possibility of obtaining high energy beams, Phys. Lett. **4**, 176 (1963).
[14] L. D. Landau and E. M. Lifshitz, *The Classical Theory of Fields* (Pergamon Press, Oxford, 1971).
[15] J. D. Jackson, *Classical Electrodynamics*, 3rd ed. (Wiley, New York, 1998).
[16] P. Sprangle, A. Ting, E. Esarey, and A. Fisher, Tunable, short pulse hard X-rays from a compact laser synchrotron source, J. Appl. Phys. **72**, 5032 (1992).
[17] K.-J. Kim, S. Chattopadhyay, and C. V. Shank, Generation of femtosecond X-rays by 90° thomson scattering, Nucl. Instrum. Methods Phys. Res., Sect. A **341**, 351 (1994).
[18] J. Gao, Thomson Scattering From Ultrashort and Ultraintense Laser Pulses, Phys. Rev. Lett. **93**, 243001 (2004).
[19] G. A. Krafft, A. Doyuran, and J. B. Rosenzweig, Pulsed-Laser nonlinear thomson scattering for general scattering geometries, Phys. Rev. E **72**, 056502 (2005).
[20] P. Catravas, E. Esarey, and W. P. Leemans, Femtosecond X-rays from thomson scattering using laser wakefield accelerators, Meas. Sci. Technol. **12**, 1828 (2001).
[21] F. V. Hartemann, D. J. Gibson, W. J. Brown, A. Rousse, K. T. Phuoc, V. Mallka, J. Faure, and A. Pukhov, Compton scattering X-Ray sources driven by laser wakefield acceleration, Phys. Rev. Spec. Top.–Accel. Beams **10**, 011301 (2007).
[22] K. Ta Phuoc, S. Corde, C. Thaury, V. Malka, A. Tafzi, J. P. Goddet, R. C. Shah, S. Sebban, and A. Rousse, All-Optical compton gamma-Ray source, Nat. Photonics **6**, 5 (2012).
[23] C. Yu, *et al.*, Ultrahigh brilliance quasi-monochromatic MeV γ-rays based on self-synchronized All-optical compton scattering, Sci. Rep. **6**, 1 (2016).
[24] H.-E. Tsai, X. Wang, J. M. Shaw, Z. Li, A. V. Arefiev, X. Zhang, R. Zgadzaj, W. Henderson, V. Khudik, G. Shvets, and M. C. Downer, Compact tunable compton X-Ray source from laser-plasma accelerator and plasma mirror, Phys. Plasmas **22**, 023106 (2015).
[25] D. P. Umstadter, All-Laser-Driven thomson X-Ray sources, Contemp. Phys. **56**, 417 (2015).
[26] A. Döpp, E. Guillaume, C. Thaury, J. Gautier, I. Andriyash, A. Lifschitz, V. Malka, A. Rousse, and K. T. Phuoc, An All-optical compton source for single-exposure x-Ray imaging, Plasma Phys. Controlled Fusion **58**, 034005 (2016).
[27] H. R. Weller, M. W. Ahmed, H. Gao, W. Tornow, Y. K. Wu, M. Gai, and R. Miskimen, Research opportunities at the upgraded HIγS facility, Prog. Part. Nucl. Phys. **62**, 257 (2009).
[28] Y. Sakai, *et al.*, Observation of redshifting and harmonic radiation in inverse compton scattering, Phys. Rev. Accel. Beams **18**, 060702 (2015).
[29] G. Sarri, D. J. Corvan, W. Schumaker, J. M. Cole, A. Di Piazza, H. Ahmed, C. Harvey, C. H. Keitel, K. Krushelnick, S. P. D. Mangles, Z. Najmudin, D. Symes, A. G. R. Thomas, M. Yeung, Z. Zhao, and M. Zepf, Ultrahigh Brilliance Multi-MeV γ-Ray Beams From Nonlinear

Relativistic Thomson Scattering, Phys. Rev. Lett. **113**, 224801 (2014).
[30] W. Yan, C. Fruhling, G. Golovin, D. Haden, J. Luo, P. Zhang, B. Zhao, J. Zhang, C. Liu, M. Chen, S. Chen, S. Banerjee, and D. Umstadter, High-Order multiphoton thomson scattering, Nat. Photonics **11**, 8 (2017).
[31] S. V. Bulanov, T. Esirkepov, and T. Tajima, Light Intensification Towards the Schwinger Limit, Phys. Rev. Lett. **91**, 085001 (2003).
[32] H. Vincenti, Achieving Extreme Light Intensities Using Optically Curved Relativistic Plasma Mirrors, Phys. Rev. Lett. **123**, 105001 (2019).
[33] F. Quéré and H. Vincenti, Reflecting petawatt lasers off relativistic plasma mirrors: A realistic path to the schwinger limit, High Power Laser Sci. Eng. **9** e6 (2021).
[34] D. H. Froula, D. Turnbull, A. S. Davies, T. J. Kessler, D. Haberberger, J. P. Palastro, S.-W. Bahk, I. A. Begishev, R. Boni, S. Bucht, J. Katz, and J. L. Shaw, Spatiotemporal control of laser intensity, Nat. Photonics **12**, 5 (2018).
[35] D. H. Froula, *et al.*, Flying focus: Spatial and temporal control of intensity for laser-based applications, Phys. Plasmas **26**, 032109 (2019).
[36] J. P. Palastro, J. L. Shaw, P. Franke, D. Ramsey, T. T. Simpson, and D. H. Froula, Dephasingless Laser Wakefield Acceleration, Phys. Rev. Lett. **124**, 134802 (2020).
[37] K. Oubrerie, I. A. Andriyash, S. Smartsev, V. Malka, and C. Thaury, Axiparabola: A New Tool for High-Intensity Optics, ArXiv:2106.06802 [Physics] (2021).
[38] S. Smartsev, C. Caizergues, K. Oubrerie, J. Gautier, J.-P. Goddet, A. Tafzi, K. T. Phuoc, V. Malka, and C. Thaury, Axiparabola: A long-focal-depth, high-resolution mirror for broadband high-intensity lasers, Opt. Lett. **44**, 3414 (2019).
[39] C. G. Durfee and H. M. Milchberg, Light Pipe for High Intensity Laser Pulses, Phys. Rev. Lett. **71**, 2409 (1993).
[40] W. Lu, C. Huang, M. Zhou, M. Tzoufras, F. S. Tsung, W. B. Mori, and T. Katsouleas, A nonlinear theory for multidimensional relativistic plasma wave wakefields, Phys. Plasmas **13**, 056709 (2006).
[41] T. Tajima and J. M. Dawson, Laser Electron Accelerator, Phys. Rev. Lett. **43**, 267 (1979).
[42] A. J. Gonsalves, *et al.*, Petawatt Laser Guiding and Electron Beam Acceleration to 8 GeV in a Laser-Heated Capillary Discharge Waveguide, Phys. Rev. Lett. **122**, 084801 (2019).
[43] N. D. Powers, I. Ghebregziabher, G. Golovin, C. Liu, S. Chen, S. Banerjee, J. Zhang, and D. P. Umstadter, Quasi-Monoenergetic and tunable X-rays from a laser-driven compton light source, Nat. Photonics **8**, 1 (2014).
[44] K. Khrennikov, J. Wenz, A. Buck, J. Xu, M. Heigoldt, L. Veisz, and S. Karsch, Tunable All-Optical Quasimonochromatic Thomson X-Ray Source in the Nonlinear Regime, Phys. Rev. Lett. **114**, 195003 (2015).
[45] H. Gao, Y. Hu, Y. Xuan, J. Li, Y. Yang, R. V. Martinez, C. Li, J. Luo, M. Qi, and G. J. Cheng, Large-Scale nanoshaping of ultrasmooth 3D crystalline metallic structures, Science **346**, 1352 (2014).
[46] D. Ramsey, B. Malaca, A. Di Piazza, M. F. P. Franke, D. H. Froula, M. Pardal, T. T. Simpson, J. Vieira, K. Weichman, and J. P. Palastro, Nonlinear Thomson Scattering with Ponderomotive Control, ArXiv:2108.04044 [Physics] (2021).
[47] J. Derouillat, A. Beck, F. Pérez, T. Vinci, M. Chiaramello, A. Grassi, M. Flé, G. Bouchard, I. Plotnikov, N. Aunai, J. Dargent, C. Riconda, and M. Grech, Smilei: A collaborative, open-source, multi-purpose particle-in-cell code for plasma simulation, Comput. Phys. Commun. **222**, 351 (2018).
[48] P. Richard, *Electromagnetic Radiation From Relativistic Electrons as Characteristic Signature of Their Dynamics* (Technische Universität Dresden, Dresden, 2012).
[49] V. I. Ritus, Quantum effects of the interaction of elementary particles with an intense electromagnetic field, J. Russ. Laser Res. **6**, 497 (1985).
[50] N. Neitz and A. Di Piazza, Stochasticity Effects in Quantum Radiation Reaction, Phys. Rev. Lett. **111**, 054802 (2013).
[51] C. N. Harvey, A. Gonoskov, A. Ilderton, and M. Marklund, Quantum Quenching of Radiation Losses in Short Laser Pulses, Phys. Rev. Lett. **118**, 105004 (2017).
[52] X. S. Geng, L. L. Ji, B. F. Shen, B. Feng, Z. Guo, Q. Yu, L. G. Zhang, and Z. Z. Xu, Quantum reflection above the classical radiation-reaction barrier in the quantum electrodynamics regime, Commun. Phys. **2**, 66 (2019).